

Hollow Multivoid Nanocuboids Derived from Ternary Ni–Co–Fe Prussian Blue Analog for Dual-Electrocatalysis of Oxygen and Hydrogen Evolution Reactions

Wook Ahn, Moon Gyu Park, Dong Un Lee, Min Ho Seo, Gaopeng Jiang, Zachary P. Cano, Fathy Mohamed Hassan, and Zhongwei Chen*

Hydrogen generation from electrochemical water-splitting is an attractive technology for clean and efficient energy conversion and storage, but it requires efficient and robust non-noble electrocatalysts for hydrogen and oxygen evolution reactions (HER and OER). Nonprecious transition metal–organic frameworks (MOFs) are one of the most promising precursors for developing advanced functional catalysts with high porosity and structural rigidity. Herein, a new transition metal-based hollow multivoid nanocuboidal catalyst synthesized from a ternary Ni–Co–Fe (NCF)-MOF precursor is rationally designed to produce dual-functionality toward OER and HER. Differing ion exchanging rates of the ternary transition metals within the prussian blue analog MOF precursor are exploited to produce interconnected internal voids, heteroatom doping, and a favorably tuned electronic structure. This design strategy significantly increases active surface area and pathways for mass transport, resulting in excellent electroactivities toward OER and HER, which are competitive with recently reported single-function nonprecious catalysts. Moreover, outstanding electrochemical durability is realized due to the unique rigid and interconnected porous structure which considerably retains initial rapid charge transfer and mass transport of active species. The MOF-based material design strategy demonstrated here exemplifies a novel and versatile approach to developing non-noble electrocatalysts with high activity and durability for advanced electrochemical water-splitting systems.

1. Introduction

Rapidly increasing international development of renewable and green energy sources has drawn widespread attention of researchers to water-splitting oxygen and hydrogen production via the electrochemical oxygen evolution reaction (OER) and hydrogen evolution reaction (HER), respectively.^[1–3] To enhance these reactions to commercially viable rates, however, high-performance electrocatalysts are required to overcome the activation energies associated with OER and HER.^[4–8] Platinum (Pt) and iridium (Ir) based materials are currently known to exhibit the highest HER and OER activities, respectively; however, their scarcity and lack of stability have made them difficult to be introduced in large-scale energy conversion and storage applications. Therefore, development of non-noble transition metal-based active catalysts with tuneable structures and compositions are currently a major energy research focal point for global implementation of clean and efficient water-splitting technologies. Recently, catalysts derived

from metal-organic frameworks (MOFs), typically synthesized using precursors consisting of transition metals and organic linkers, have emerged as promising active and inexpensive electrocatalysts due to their intrinsic advantages of high porosity, 3D structures, and compositional flexibility. In particular, MOFs with organic ligands containing carbon, nitrogen, and sulfur atoms coordinated to transition metal centers have been reported to form 3D and uniformly porous structures, resulting in considerably increased active surface area and enhanced physical properties. These MOFs, often composed of transition metal atoms such as nickel, cobalt, and iron, and heteroatoms such as nitrogen, sulfur, and phosphorus are characterized by strong interactions between them, which can serve as electrocatalytically active sites for HER and OER.^[9–17]

The advantages of MOF-derived active materials in advanced energy conversion and storage applications have been recently applied to efficient electrocatalysts for fuel cells, metal–air batteries, and electrolyzers.^[6,15,17–29] For example, Gadipelli et al. recently reported a design route for the

Prof. W. Ahn
Department of Energy Systems Engineering
Soonchunhyang University
22 Soonchunhyang-ro, Shinchang-myeon, Asan-si, Chungcheongnam-do
31538, South Korea

Prof. W. Ahn, M. G. Park, Dr. D. U. Lee, Dr. M. H. Seo, Dr. G. Jiang,
Z. P. Cano, Dr. F. M. Hassan, Prof. Z. Chen
Department of Chemical Engineering
University of Waterloo
Waterloo Institute for Nanotechnology
200 University Avenue West, Waterloo, Ontario N2L 3G1, Canada
E-mail: zhwchen@uwaterloo.ca

Dr. M. H. Seo
Hydrogen & Fuel Cell Center
New & Renewable Energy Research Division
Korea Institute of Energy Research (KIER)
20–41 Sinjaesaengneogi-ro, Haseo-myeon, Buan-gun, Jellabuk-do
56332, South Korea

 The ORCID identification number(s) for the author(s) of this article can be found under <https://doi.org/10.1002/adfm.201802129>.

DOI: 10.1002/adfm.201802129

synthesis of MOF-derived electrocatalysts, in which zeolitic imidazolate framework was used as the template.^[30] The resulting MOF catalyst containing active Co–N–C species demonstrated efficient ORR and OER activities. Yu et al. reported an active OER electrocatalyst based on porous carbon-coated nickel phosphides (NiP) prepared using Ni-based prussian blue analog (PBA) nanoplates as a template.^[31] The structural advantages of MOFs allowed the NiP catalyst to demonstrate superior electrocatalytic activity toward OER compared to NiO and Ni(OH)₂ counterparts. Despite these electrocatalyst developments, however, bifunctional MOF-derived electrocatalysts active toward both HER and OER for water-splitting applications have rarely been reported to the best of our knowledge.

In this study, we introduce novel MOF-containing Ni–Co–Fe transition metal centers (denoted NCF-MOF) as a dual-function water-splitting catalyst for enhancing HER and OER activities. The morphology of the catalyst is revealed to exhibit a nanocuboid structure with multiple mesosized and micro-sized pores prepared via a facile synthesis procedure. Transition metal-based PBA nanocubes with a chemical formula $M_x^{II}[M_y^{III}(\text{CN})_6]_z \cdot n\text{H}_2\text{O}$, where M^{II} and M^{III} are divalent and trivalent transition metal cations, respectively, were selected as MOF precursors to obtain unique compositions and multi-hollow nanocuboid structures.^[12,32] Specifically, PBA nanocube precursors containing nickel, cobalt, and iron were utilized to maintain the general nanocuboidal structure, while optimizing the composition of transition metal centers for efficient OER and HER activities. This makes NCF-MOF one of the most promising nonprecious electrocatalysts for water-splitting applications due to several material advantages including i) significantly extended active surface area with high porosity and robust structure, ii) active nitrogen species formed during facile synthesis, and iii) favorably tuned electronic structure by combining active transition metals having different number of outer electrons.

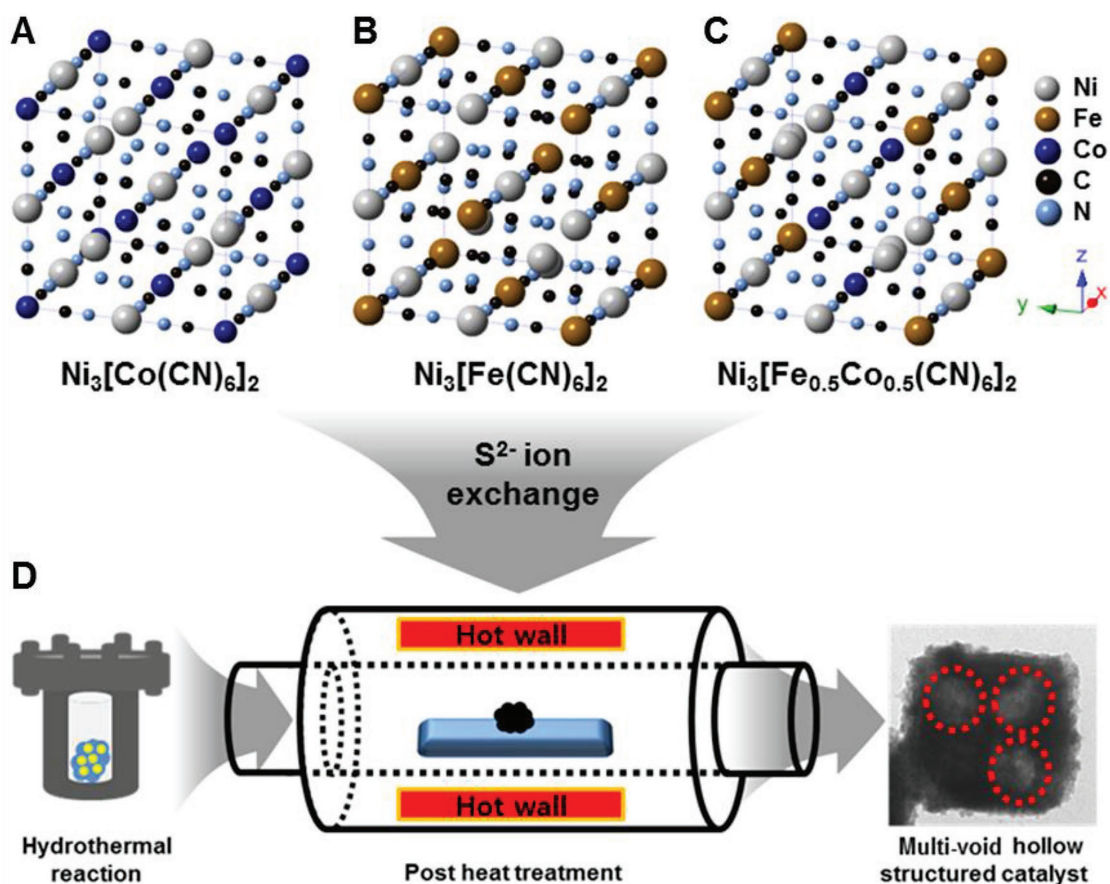
These main electrocatalytic contributors that affect OER and HER were successfully obtained through careful selection of PBA precursors and the facile synthesis procedure. Furthermore, the NCF-MOF catalyst exhibited excellent electrochemical stability, which is attributed to its highly uniform and rigid porous nanocuboidal structure that allows rapid charge transfer and mass transport of active species to be maintained. The dual-function of the catalyst and its stability was confirmed by three-electrode half-cell evaluations, and moreover was integrated onto nickel-foam supports for practical demonstrations of efficient and stable water-splitting electrodes.

2. Results and Discussion

A schematic illustration of the synthesis procedure of multi-void MOF nanocuboid electrocatalysts using PBA nanocube precursors is presented in **Scheme 1**. The PBA precursors are composed of transition metal ions (Ni, Fe, and/or Co) and cyanide (CN) groups in the face-centered cubic (FCC) crystal packing arrangement.^[33,34] The PBA precursors used in this study consisted of different combinations of transition metal centers, namely, Ni/Co (NC-PBA, Scheme 1A), Ni/Fe (NF-PBA, Scheme 1B), and Ni/Co/Fe (NCF-PBA, Scheme 1C).

These nanocube precursors were subjected to sulfur ion (S^{2-}) exchange, and then crystallized via hydrothermal treatment followed by postheat treatment (Scheme 1D) to form highly crystalline multivoid nanocuboids. This hierarchical hollow nanocuboidal MOF structure is very interesting for electrocatalysis of OER and HER due to a possible increased number of active sites from enlarged surface area. The exact morphology of the MOF catalysts, however, largely depends on the type of transition metal centers present in the PBA precursor. For example, NC-MOF (NC-PBA precursor shown in Figure S1A,B, Supporting Information) showed nanocuboidal structures with an average size of 400 nm and relatively large pores on each face (**Figure 1A,B**), while NF-MOF (NF-PBA precursor shown in Figure S1C,D, Supporting Information) showed uniformly sized cuboidal structures with an average size of 160 nm, maintaining the initial PBA precursor morphology (Figure 1D,E). NCF-MOF (NCF-PBA precursor shown in Figure S1E,F, Supporting Information) exhibited general cuboid morphology with an average size of 180 nm and roughened surfaces (Figure 1G,H). Interestingly, NF-PBA and NCF-PBA precursors were relatively smaller than NC-PBA, probably due to the presence of Fe ions. Moreover, the large pores observed in NC-MOF possibly formed during the hydrothermal processes due to very rapid ion exchanging between $[\text{Co}(\text{CN})_6]^{3-}$ and S^{2-} ions, resulting in breakage of outer metal ions from the cuboid structures.^[34] This led to the formation of NC-MOF with considerable shape change from the compact cuboid to porous structures. Unlike the significant morphological changes observed with NC-MOF from its precursor, NF-MOF and NCF-MOF largely maintained their nanocuboidal structures. Only a slight morphology change observed with NF-MOF (roughening of its surface) was likely due to relatively lower ion exchanging power of $[\text{Fe}(\text{CN})_6]^{3-}$ with S^{2-} anions (compared to that of $[\text{Co}(\text{CN})_6]^{3-}$ in the case of NC-MOF), resulting in significantly less ion exchange and minimal morphological change. NCF-MOF is particularly interesting because of the presence of both $[\text{Co}(\text{CN})_6]^{3-}$ and $[\text{Fe}(\text{CN})_6]^{3-}$ having different ion exchanging rates which led to partial replacement with S^{2-} ions, resulting in an externally roughened surface, and internally having multiple voids within a single nanocuboid, which will be further discussed in the following section.

Transmission electron microscopy (TEM) analysis was conducted to reveal the internal morphological features of the MOF catalysts. NC-MOF under TEM revealed that the large pores observed on all faces of the nanocuboids were in fact interconnected, resulting in a hollow core (Figure 1C). NF-MOF, on the other hand, maintained the nonporous nanocuboidal structure from its precursor (Figure 1F), consistent with the scanning electron microscopy (SEM) observations. TEM observations of NCF-MOF revealed spots within a single nanocuboid with different brightness (Figure 1I), indicative of multiple void formations during the ion exchanging reaction. These morphological differences again highlight different ion exchanging rates of each PBA precursor, and how they affect the final external and internal structures of the MOF catalysts. In terms of crystal structure, X-ray diffraction (XRD) characterization revealed that the pattern obtained from NC-MOF closely matches with that of NiS (JCPDS: 77-1624) (Figure S2A, Supporting Information), indicative of near-complete



Scheme 1. A–D) Schematic illustration of MOF electrocatalyst synthesis procedure using PBA nanocube precursors to form multivoid hollow nanocuboidal MOF catalyst.

exchange of $[\text{Co}(\text{CN})_6]^{3-}$ with S^{2-} ions, as expected from the above microscopic analyses.^[32] The obtained patterns of NF-MOF (Figure S2B, Supporting Information) and NCF-MOF (Figure S2C, Supporting Information), on the other hand, matched the typical characteristic peaks of PBA, due to relatively lower degree of $[\text{Fe}(\text{CN})_6]^{3-}$ exchanged with S^{2-} anions, as conjectured based on morphological observations.^[34] Scanning TEM (STEM) of a single NC-MOF nanocuboid was used to obtain energy-dispersive X-ray spectroscopy (EDS) line-scans through the mid-section (Figure S3A, Supporting Information) and the edge (Figure S3B, Supporting Information). The elements detected in the nanocuboids, Ni, Co, Fe, C, N, and S, are indicated by different colors of the line-scan with the respective intensity corresponding to the amount of each element, which are separately plotted in Figure S5 (Supporting Information). The plots clearly show that the intensities of all detected elements are relatively higher at both ends of the plot compared to the center, which confirms the internally connected porous structure with a hollow core. From high-resolution transmission electron microscopy (HRTEM) images obtained from NC-MOF (Figure S3C,D, Supporting Information), selected area electron diffraction (SAED) patterns were also obtained at the center and the edge of the nanocuboids, both of which reveal FCC lattice structures. In terms of composition, dark-field TEM (DFTEM) and elemental mapping were conducted to verify

the compositional characteristics of NC-MOF, as presented in Figure S3E–J (Supporting Information). The elemental maps indicate that NC-MOF is composed of nickel, nitrogen, sulfur, carbon, and residual cobalt, which clearly shows that most of the $[\text{Co}(\text{CN})_6]^{3-}$ was in fact exchanged by S^{2-} ions, leading to the formation of NiS with hollow-core morphology. The intensity of each elemental map is in good agreement with the EDS line-scan measurements.

Meanwhile, NF-MOF exhibited a much denser internal cuboidal core compared to that of NC-MOF, based on the STEM images shown in Figure S4A,B (Supporting Information), while SAED patterns obtained at the center (Figure S4C, Supporting Information) and the edge (Figure S4D, Supporting Information) of the nanocuboid indicate a polycrystalline FCC structure. Based on both EDS line-scan (Figures S4A,B and S6, Supporting Information) and DFTEM elemental mapping (Figure S4E–J, Supporting Information) results, relatively larger amounts of nickel and iron were detected within NF-MOF with lower amounts of carbon, sulfur, and nitrogen uniformly distributed along both the center and edge parts. The low amount of sulfur detected is particularly important for verifying that the rate of ion exchange of $[\text{Fe}(\text{CN})_6]^{3-}$ with S^{2-} ions was indeed slower than that of $[\text{Co}(\text{CN})_6]^{3-}$ observed with NC-MOF. Interestingly, higher amounts of nitrogen and carbon detected compared to NC-MOF are likely due to the decomposition of the

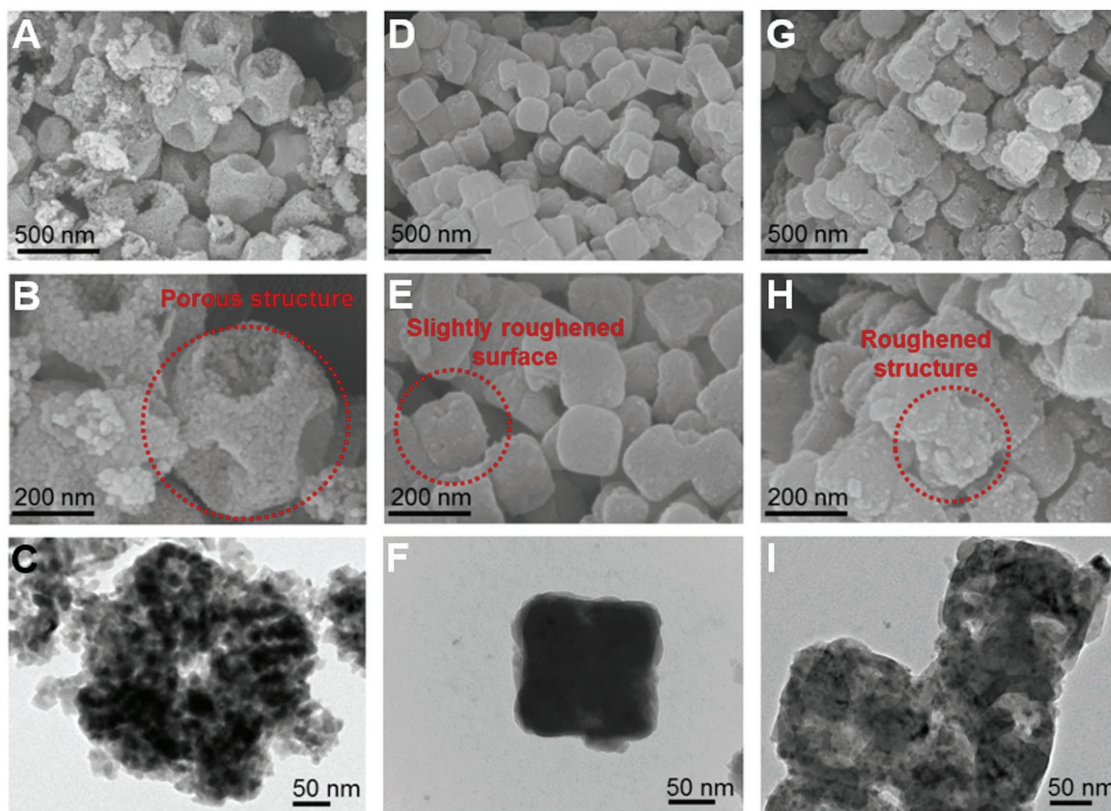


Figure 1. A,B,D,E,G,H) SEM and C,F,I) TEM images of various MOF morphologies. A–C) NC-MOF with large face-centered pores, D–F) NF-MOF nanocuboids, and G–I) NCF-MOF nanocuboids with roughened surface.

cyanide groups in the PBA precursor during the heat-treatment process, which will be discussed in more detail later.

Based on the above characterizations of NC-MOF and NF-MOF, it is clear that combining $[\text{Co}(\text{CN})_6]^{3-}$ and $[\text{Fe}(\text{CN})_6]^{3-}$ anions having different rates of ion exchanging capabilities can lead to a unique morphology and composition for NCF-MOF as observed in microscopic analyses. Compared to NC-MOF and NF-MOF, the results obtained from EDS line-scans (Figure 2A,B; Figure S7, Supporting Information) and DFTEM elemental mapping (Figure 2E–K) of NCF-MOF show that the three transition metals (nickel, cobalt, and iron) are uniformly distributed along the middle and the edge of nanocuboids, indicating that $[\text{Co}(\text{CN})_6]^{3-}$ and $[\text{Fe}(\text{CN})_6]^{3-}$ anions were only partially exchanged by S^{2-} ions. This partial ion exchange led to the formation of multiple voids within a single nanocuboid, where the exchange most likely progressed from the surface $[\text{Co}(\text{CN})_6]^{3-}$ anions to the sites in the core. Accordingly, NCF-MOF is characterized by having larger interconnected pores in the core with smaller pores near the faces of the nanocuboid, resulting in a multilevel porous structure. The crystal structure of NCF-MOF confirmed by SAED patterns obtained from HRTEM images at the face center (Figure 2C) and the edge (Figure 2D) reveal $[001]$ and $[111]$ orientations, respectively, as indicated by a series of bright dots from strongly diffracted crystal planes of the nanocuboid, corresponding to a typical FCC structure.

The observed porosity of NF-MOF and NCF-MOF was quantified by measuring N_2 adsorption/desorption isotherms and

pore size distribution, as presented in Figure S8 (Supporting Information). Based on the N_2 isotherms, both NF-MOF and NCF-MOF show a clear hysteresis loop in the high pressure range from 0.6 to 1.0, indicating the presence of mesopores.^[21] However, NCF-MOF adsorbed a much greater volume of N_2 resulting in a $50.7 \text{ m}^2 \text{ g}^{-1}$ Brunauer–Emmett–Teller (BET) surface area, compared to only $27.4 \text{ m}^2 \text{ g}^{-1}$ obtained with NF-MOF. In terms of the pore size distribution, despite both nanocuboids having micropores (under 2 nm) and mesopores (over 2 nm), NCF-MOF was found to have two times the accumulative pore volume compared to NF-MOF (0.29 vs 0.14 cc g^{-1}) due to the presence of a significantly large number of mesopores. This direct evidence that NCF-MOF has enhanced specific surface area signifies a potential increase in the number of active sites for electrocatalytic processes which can greatly improve OER and HER activities.

The composition of the MOF nanocuboid catalysts was further analyzed by X-ray photoelectron spectroscopy (XPS). The survey spectrum of NF-MOF revealed Ni, Fe, O, N, and S, while that of NCF-MOF revealed Ni, Co, Fe, O, N, C with a low intensity S peak (Figure S9A, Supporting Information). By contrast, the spectrum of NC-MOF revealed Ni, O, C with a high intensity S peak, indicating again that most of the $[\text{Co}(\text{CN})_6]^{3-}$ was ion exchanged with S^{2-} ions leading to the formation of hollow-centered NiS nanocuboids, as discussed earlier. The high-resolution spectrum of selected elements present in the nanocuboid catalysts was deconvoluted to verify the oxidation states. The high-resolution Ni 2p (Figure S9B, Supporting

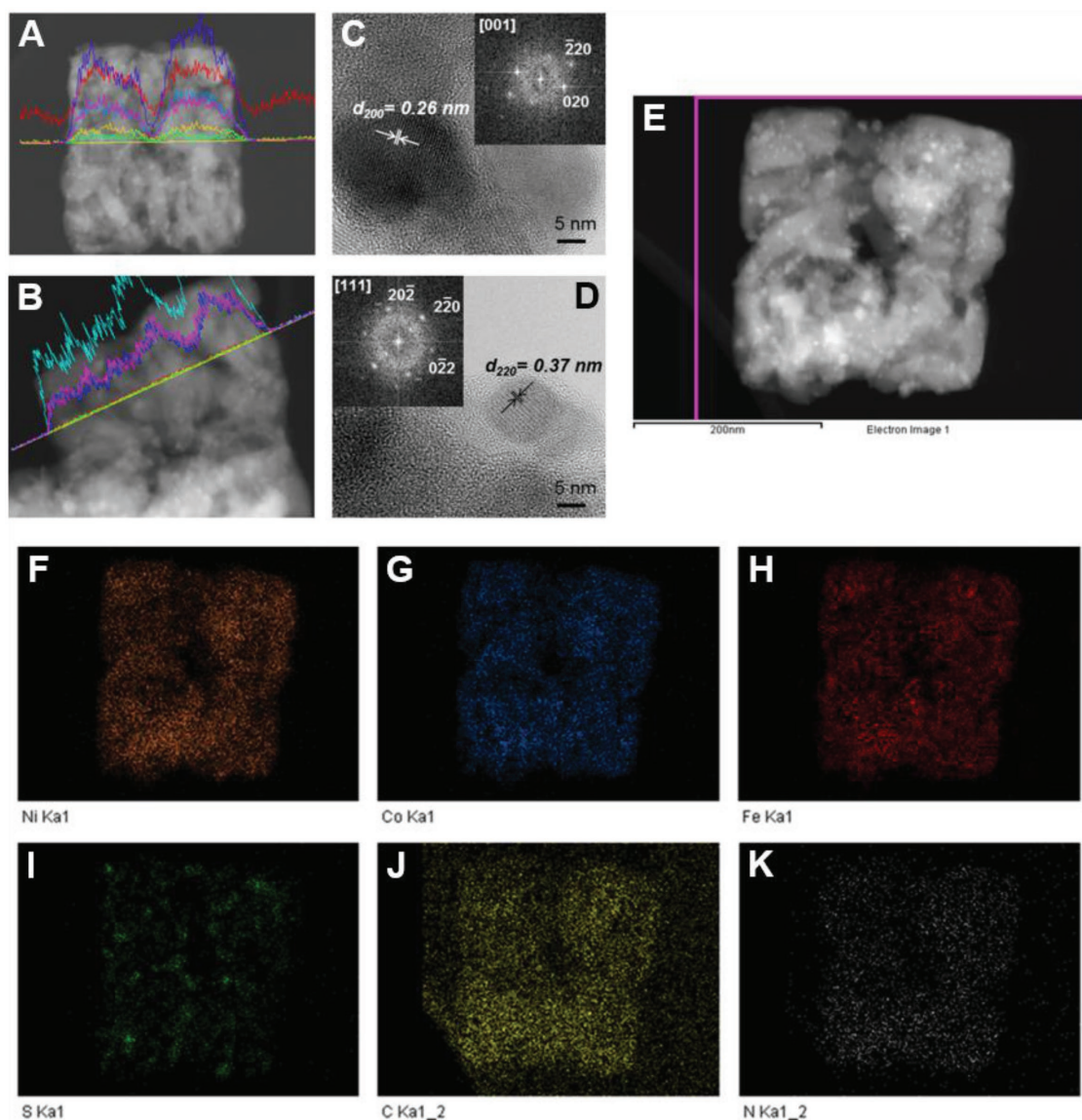


Figure 2. TEM analysis of NCF-MOF. A,B) STEM images with EDS line-scans obtained along the middle and edge of NCF-MOF, C,D) HRTEM images and SAED patterns obtained at the center and the edge of NCF-MOF, E) DFTEM image of NCF-MOF, and the obtained elemental maps of F) Ni, G) Co, H) Fe, I) S, J) C, and K) N.

Information) and S 2p (Figure S9C, Supporting Information) spectra of NC-MOF show peaks found at binding energies that correspond to NiS and Ni₃S₂.^[35] While Ni₃S₂ was detected from the XPS analysis, no peaks that corresponded to this impurity in the XRD pattern of NC-MOF were observed, which indicates that its amount may be negligibly small due to a near-complete ion exchange of [Co(CN)₆]³⁻ with S²⁻ during the hydrothermal reaction. Based on the analysis of Ni 2p (Figure S9D, Supporting Information) and Fe 2p (Figure S9E, Supporting Information) signals from NF-MOF, it was found to mainly consist of Ni in 2+ states, and Fe with 27% of 3+, and 73% of 2+ states, leading to a possible chemical formula of Ni_x^{II}[Fe_y^{II}Fe_z^{III}(CN)₆]₂. NCF-MOF, on the other hand, was found to be composed of Ni in 2+ states (Figure 3A), Fe in 43% and 57% of 2+ and 3+ states (Figure 3B), and Co in 17% and 83% of 2+ and 3+ states

(Figure 3C), respectively. Based on the high resolution Ni 2p peak, it was found that a small quantity of NiS formed (5.4%), while only low intensity multiplet NiS peaks were observed in the high-resolution S 2p spectrum of NCF-MOF (Figure 3D), which are ascribed to the S²⁻ ions partially replacing [Co(CN)₆]³⁻ during ion exchange, consistent with the above XRD and microscopic characterization. However, the lack of characteristic NiS peaks observed in the XRD patterns of NF-MOF and NCF-MOF indicate that the small quantities of NiS in these samples were amorphous. These oxidation states of the transition metals determined from XPS analysis are related to the number of valence electrons, which in turn determines the electronic state and the number of electrons that are involved during electrocatalytic reactions.^[36–39] Recently, several studies revealed that valence electrons of transition metals are highly related

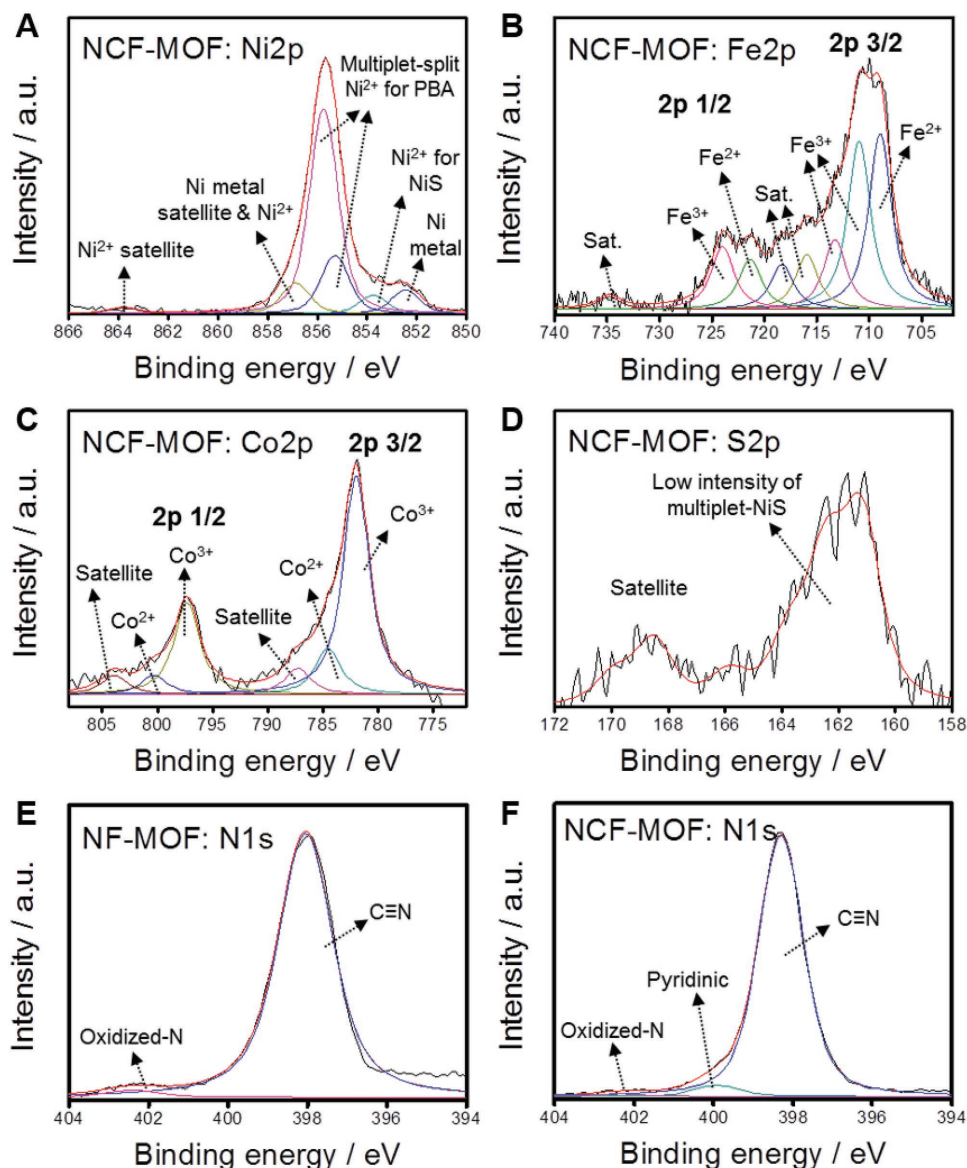


Figure 3. Deconvoluted high-resolution XPS spectra obtained from NCF-MOF. A) Ni 2p, B) Fe 2p, C) Co 2p, and D) S 2p. Deconvoluted high-resolution XPS N 1s spectra of E) NF-MOF and F) NCF-MOF.

to the trends in adsorption energies of intermediates of the OER.^[36,38,39] In these works, metals and corresponding metal oxides were studied and the correlation between the number of outer electrons and the adsorption energy of the intermediates such as *OH, *O, and *OOH during oxygen electrocatalysis were systematically investigated. The trends demonstrated the higher the number of outer electrons, the larger the adsorption energies of the oxygen intermediates leading to higher overpotentials toward OER. Furthermore, the trends remained similar across different structures of metals, metal monoxides, as well as perovskite oxides. In the current study, based on the oxidation states determined from the XPS analysis above, the outer electron number of Fe in NF-MOF was found to be 5.73, while those of Fe and Co in NCF-MOF were found to be 2.71 and 2.78, respectively, adding up to 5.49 (detailed calculations in the Supporting Information). Considering the number of outer

electrons, it can be implied that the active surface of NF-MOF has relatively high adsorption strength with the oxygen intermediates leading to a lower OER electroactivity. Valence electrons of NCF-MOF finely tuned by the combination of active Co and Fe metal ions, on the other hand, would render relatively weaker adsorption of the oxygen intermediates, resulting in lower overpotential toward OER and more facilitated evolution of gaseous oxygen. The improved OER performance resulting from this explanation will be demonstrated by electrochemical evaluation in the next section. The obtained XPS N 1s spectra of NF-MOF and NCF-MOF were deconvoluted to verify the type of nitrogen species present in each electrocatalyst, since N-doping has been reported to facilitate HER. It is noted that the N 1s peak was not detected with NC-MOF, as shown in Figure S9A (Supporting Information) due to near-complete exchange of $[\text{Co}(\text{CN})_6]^{3-}$ with S^{2-} ions. The N species found in

NF-MOF predominantly existed as $C\equiv N$ (98.7%), which was from the remaining unexchanged $[Fe(CN)_6]^{3-}$ anions, and the rest as oxidized-N (1.9%) formed during the hydrothermal process (Figure 3E). Interestingly, NCF-MOF, in addition to having $C\equiv N$ (94.7%) and oxidized-N (0.9%), also contained pyridinic N species (4.24%) (Figure 3F). This unique N-doping of NCF-MOF is ascribed to the decomposition of free CN^- groups generated in solution during the ion exchanging process. In fact, previous studies reported that $Fe(CN)_6$ is effective in dissociating metal cyanides, decomposing CN^- in soil at temperatures lower than $100\text{ }^\circ\text{C}$.^[40] Likewise, $Ni_3[Fe(CN)_6]_2$ groups in NCF-MOF most likely facilitated the dissociation of free $[Co(CN)_6]^{3-}$ ions in solution, producing CN^- ions which oxidize to CNO^- and then further decompose to NH_3 , a common N-doping source.^[40] This N-doping is unique to NCF-MOF because the remaining $Fe(CN)_6$ groups in the nanocuboid act as a catalyst to facilitate the decomposition of CN^- groups of the $[Co(CN)_6]^{3-}$ anions freed into the solution after ion exchanging with S^{2-} . Specifically, 9.85% of $[Co(CN)_6]^{3-}$ in NCF-MOF was ion exchanged with S^{2-} , and 86% of the freed CN^- groups were found to be used as the N source based on the XPS analysis. This result is also consistent with the EDS line-scan analysis presented above, which clearly showed the presence of both nitrogen and carbon along the middle and edges of NCF-MOF.

This unique N-doping within NCF-MOF which formed during the decomposition of CN^- leads to more favorable HER electrochemical activity due to the synergistic effect with neighboring transition metals, such as Ni, Co, and Fe,^[15,18,41,42] which will be demonstrated in the next section.

The electrochemical OER and HER activities of the MOF electrocatalysts were investigated using a typical three-electrode half-cell configuration with conventional glassy carbon rotating disk electrode (RDE) with 0.2 mg cm^{-2} of catalyst loading in N_2 -saturated 0.1 M KOH electrolyte. Based on the HER polarization curves, NCF-MOF demonstrated the lowest overpotential (most positive absolute potential) of 0.27 V (see measurement details in the Experimental Section), compared to those of NF-MOF and NC-MOF (0.34 and 0.39 V , respectively) at a current density of -10 mA cm^{-2} (Figure 4A). This excellent HER activity of NCF-MOF is comparable to some of the best known nonprecious HER catalysts in the basic condition (See Table S1 in the Supporting Information), which is attributed to the reduced energy barrier for HER due to the N-doped species uniquely found in NCF-MOF.^[15,40,42] Based on the previous study, nitrogen doping leads to a decrease in $\Delta G(H^*)$ by providing improved adsorption for H^* onto the active sites.^[43–46] Additionally, since the properties of materials are highly sensitive to their morphology and structure, the unique structure

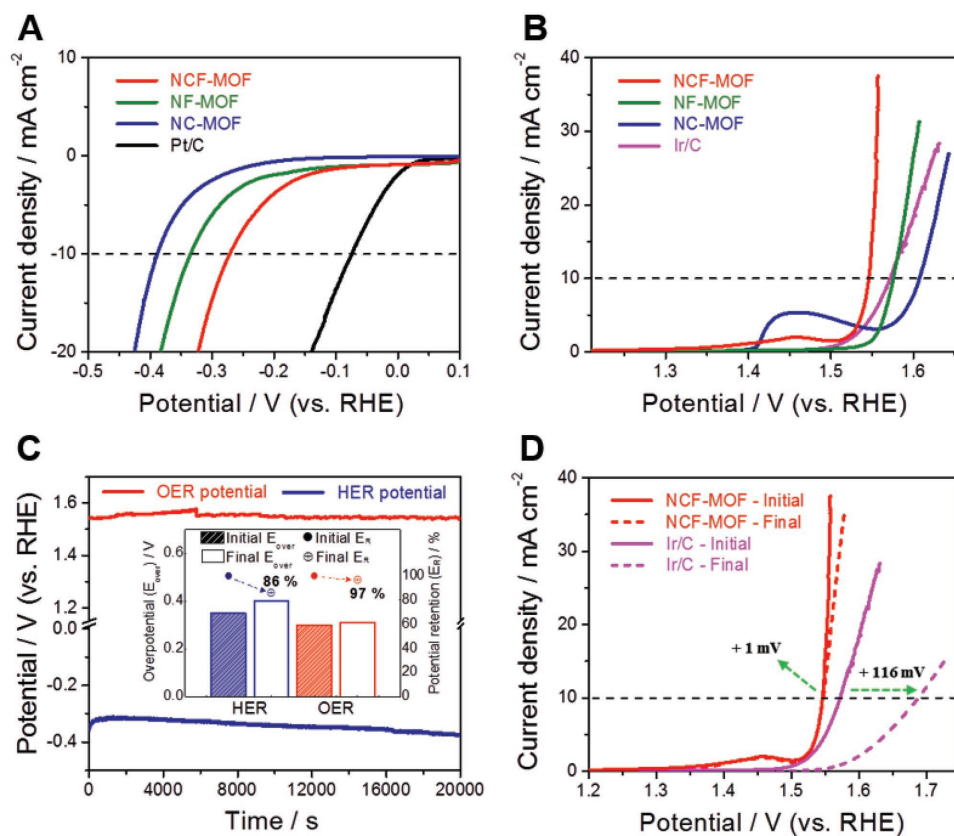


Figure 4. Electrochemical evaluations of MOF catalysts. A) HER and B) OER curves obtained with MOF catalysts and precious metal-based benchmark catalysts. C) Chronopotentiometry (ν - t) plot obtained with NCF-MOF at a fixed applied current density of -20 mA cm^{-2} for HER (blue line) and 20 mA cm^{-2} for OER (red line). The inset of (C) shows the changes in the overpotentials during chronopotentiometric HER and OER tests (bar graphs), and the corresponding potential retentions (dot graphs). D) OER polarization curves of NCF-MOF and Ir/C before (solid lines) and after (dashed lines) 1000 CV cycles.

as well as the N-doped surface of NCF-MOF probably further contributes to its highly active and durable HER activity.^[47] As an effective dual-function catalyst, NCF-MOF also showed the lowest OER overpotential of 0.32 V obtained at 10 mA cm⁻² even compared to that of precious-metal benchmark catalyst Ir/C (Figure 4B), while it is superior compared to the recently reported nonprecious active OER electrocatalysts (Table S1, Supporting Information). Specifically, NF-MOF, NC-MOF, and Ir/C demonstrated 30, 60, and 20 mV higher overpotentials, respectively. The significant OER activity of NCF-MOF is also comparable to the best reported values of recently developed nonprecious metal-based OER electrocatalysts (see Table S1 in the Supporting Information). The enhanced OER activity of NCF-MOF is attributed to the favorably tuned electronic structure by combining the number of outer electrons of active Co and Fe metal ions, which leads to reduced adsorption strength with the oxygen intermediates such as *O, *OH, and *OOH, as discussed above. To emphasize excellent OER and HER capabilities of NCF-MOF, the catalysts were also loaded onto practical nickel foam electrodes (NFEs) commonly used in water-splitting cells (see electrode preparation details in the Experimental Section). Under HER conditions, NCF-MOF again demonstrated the lowest overpotential of 0.16 V obtained at a current density of -30 mA cm⁻², compared to those of NF-MOF and NC-MOF (0.25 and 0.30 V, respectively) (Figure 5A). Additionally, the Tafel plots obtained from the HER curves resulted in the smallest slope for NCF-MOF (114 mV dec⁻¹) compared to those

of NF-MOF and NC-MOF (157 and 168 mV dec⁻¹, respectively) (Figure 5B), signifying much faster kinetics during the HER. Similarly, the lowest OER overpotential was obtained with the NCF-MOF catalyst loaded on a NFE, demonstrating 0.48 V obtained at 30 mA cm⁻², which is 110 and 160 mV lower than those of NF-MOF and Ir/C, respectively (Figure 5C). The OER Tafel analysis also showed the smallest slope of 49 mV dec⁻¹ for NCF-MOF, compared to those of NF-MOF, NC-MOF, and Ir/C (119, 99, and 73 mV dec⁻¹, respectively) (Figure 5D), signifying the highest kinetics during the OER on NCF-MOF. As a control, a bare nickel foam without any catalyst loading showed current densities associated with HER and OER but at much higher overpotentials and with significantly lower magnitudes compared to the catalyst-loaded counterparts (Figure S10, Supporting Information).

In addition to the excellent dual OER and HER activities of NCF-MOF, its electrochemical stability was investigated by conducting chronopotentiometry (CP). When held at -20 mA cm⁻², the NCF-MOF electrode exhibited an initial HER potential of -0.34 V versus reversible hydrogen electrode (RHE), and a voltage loss of only 0.05 V after 20 000 s (Figure 4C). During CP under OER conditions, the NCF-MOF electrode held at 20 mA cm⁻² demonstrated an initial OER potential of 1.53 V versus RHE (0.3 V of OER overpotential). After 20 000 s, only a 0.01 V increase in the OER potential was observed, leading to 97% of potential retention, demonstrating very slight degradation during the durability test (Figure 4C, inset). Conducting

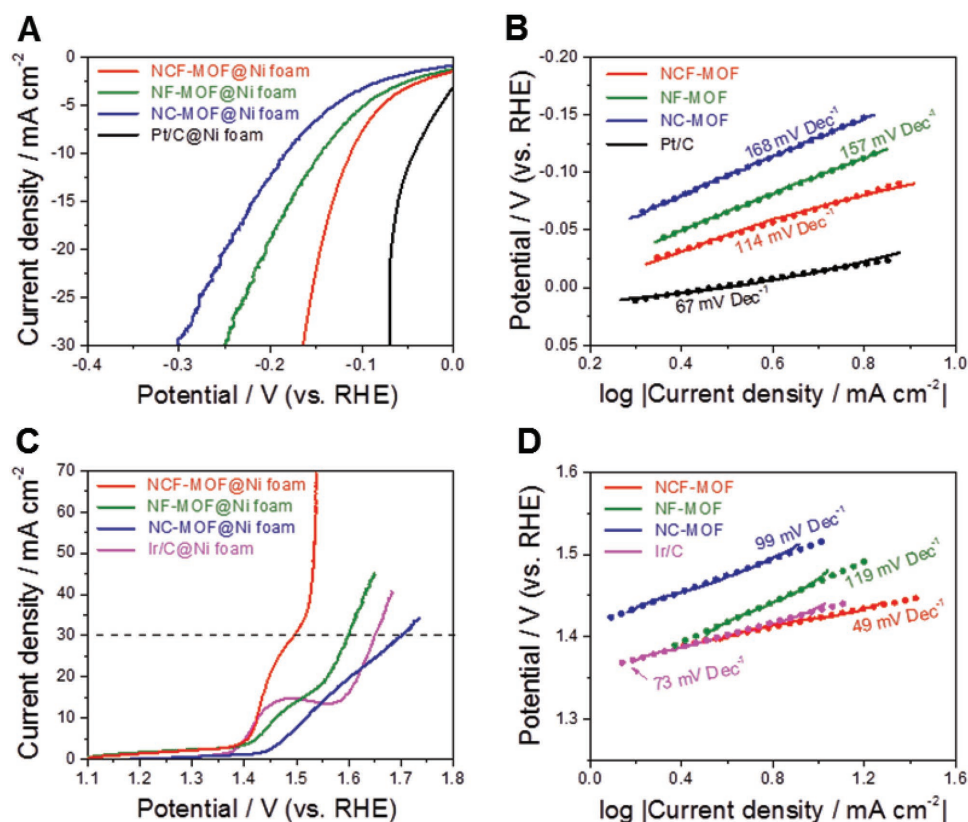


Figure 5. Electrochemical evaluations of MOF catalyst-loaded nickel foam electrodes. A) HER polarization curves, and B) HER Tafel slopes obtained with NCF-MOF, NF-MOF, NC-MOF, and Pt/C. C) OER polarization curves, and D) OER Tafel slopes obtained with NCF-MOF, NF-MOF, NC-MOF, and Ir/C.

electrochemical stability via cyclic voltammetry (CV), as commonly done in the field, further confirmed the considerably high electrochemical stability of NCF-MOF, with Ir/C used as the benchmark catalyst for comparison.^[22,23,48] Initially, NCF-MOF displayed a significantly lower (superior) OER potential of 1.54 V versus RHE at 10 mA cm⁻² in comparison to 1.57 V obtained with Ir/C (Figure 4D). After 1000 CV cycles in the highly oxidative potential window of 1.2 to 1.75 V versus RHE, NCF-MOF showed only 1 mV of OER potential loss (99% potential retention), while Ir/C showed a significantly greater potential loss of 116 mV (66% potential retention). The structural stability of NCF-MOF after the long term durability tests in both OER and HER potential regions was verified by performing TEM characterization in terms of morphology (Figure S11, Supporting Information). The overall nanocuboid morphology of NCF-MOF (A, B are before durability testing) was observed to be maintained after OER (C, D) and HER (E, F) durability tests in the alkaline electrolyte. The edges were observed to be somewhat roughened which is likely due to the formation of metal hydroxides where the metal sites tend to be undercoordinated, which is consistent with the results reported in the literature.^[49,50]

The extended electrochemical stability observed with NCF-MOF during HER and OER is likely attributed to the highly rigid porous structure consisting of the robust metal–organic-frameworks, which enables it to mostly retain the initial electrocatalytic activities via retaining the framework during rigorous H₂ and O₂ gas bubbling. Additionally, during OER, even lower overpotential for NCF-MOF than the precious benchmark Ir/C catalyst leads to significantly reduced oxidation of active metals while the catalyst undergoes relatively reduced carbon-corrosion. It can be concluded that the solid and interconnected porous structure via the ternary transition metal-based MOF design as well as the harmonized effects between Co and Fe metals in the framework achieved synergistic improvements in electrocatalytic activities and durability for both OER and HER.

3. Conclusion

In summary, multivoid nanocuboidal MOF catalysts prepared by a facile coprecipitation and postheat treatment process were found to demonstrate high electrocatalytic activities as well as stability toward both OER and HER. The morphology and composition of the MOF catalysts were investigated by taking advantage of different ion exchanging rates of [Co(CN)₆]³⁻ and [Fe(CN)₆]³⁻ anions in PBA precursors with S²⁻ ions. The formation of unique nanocuboid morphology with high internal porosity of NCF-MOF is attributed to the ion exchanging of [Co(CN)₆]³⁻ with S²⁻ ions, while relatively unreactive [Fe(CN)₆]³⁻ remains stagnant but facilitates the decomposition of free CN⁻ groups to induce nitrogen-doping, forming HER active pyridinic nitrogen species. Additionally, the unique combination of the two precursors containing Co and Fe results in a favorably tuned electronic structure, leading to relatively reduced adsorption energy of the oxygen intermediates, which is critical for lowering the overpotential toward OER and facilitating the evolution of gaseous oxygen. In terms of electrochemical stability, after 20 000 s of operation NCF-MOF retained 86% and 97% of its HER and OER potentials, respectively, and far exceeded the

stability of precious metal-based benchmark catalyst Ir/C, demonstrating minimal OER potential losses after 1000 CV cycles in a highly oxidative potential window. Furthermore, the TEM analysis verified the high structural stability of NCF-MOF after the long term durability tests conducted in both OER and HER potential regions. This work exemplifies novel electrocatalyst development with high activity and durability for next generation energy conversion and liquid-fuel production technologies including electrochemical water-splitting cells.

4. Experimental Section

Synthesis of Precursor and MOF Materials: The facile preparation procedure of MOF electrocatalysts is presented in Scheme 1. The PBA nanocubes, which were utilized as precursors, were synthesized by the coprecipitation method, where the precursors included Ni and Co (NC-PBA), Ni and Fe (NF-PBA), or Ni, Fe, and Co (NCF-PBA) ions. For the first precursor, 0.6 mmol of nickel nitrate and 0.9 mmol of sodium citrate were first dissolved in 20 mL of Milli-Q water. Next, 0.4 mmol of potassium hexacyanoferrate (III) was dissolved in another 20 mL of Milli-Q water. The two solutions were then mixed and vigorous stirring was conducted for 12 h to synthesize the NF-PBA precursor with uniformly distributed particle sizes. The NC-PBA and NCF-PBA precursors were synthesized by the same method, except for the use of 0.4 mmol potassium hexacyanocobaltate (III) solution for NC-PBA, and a mixed solution of 0.2 mmol potassium hexacyanocobaltate (III) and 0.2 mmol potassium hexacyanoferrate (III) for NCF-PBA. It is well known that the citrate ions prohibit the precipitation reaction from forming large-sized particles. Therefore, a sufficient reaction time was required to prepare uniformly distributed precursors with small sized particles.^[31] The MOFs were obtained from the as-prepared PBA precursors through a simple hydrothermal reaction with the addition of sodium sulphide (Na₂S). 100 mg of PBA precursor and 200 mg of Na₂S were mixed in 100 mL of ethanol and transferred into a Teflon liner and stainless-steel autoclave. The hydrothermal reaction was carried out at 100 °C for 6 h to induce sufficient ion exchange. Then, the intermediate product was washed, dried, ground, and heat treated at 300 °C in Ar atmosphere for 3 h to form highly crystalline MOFs. The black recrystallized MOFs were pulverized and dried in a vacuum oven at 70 °C for 12 h. The final MOF products containing Ni/Co, Ni/Fe, and Ni/Co/Fe centers were denoted NC-MOF, NF-MOF, and NCF-MOF, respectively.

Physical Characterization: In order to confirm the crystal structures of the synthesized materials, XRD (AXS D8 Advance, Bruker) was carried out with Cu K α radiation ($\lambda = 1.5405 \text{ \AA}$) in the 2 θ range of 10°–80° with 0.02° intervals, at a 0.02° min⁻¹ scanning rate. The morphology and elemental distribution of the as-prepared PBA precursors and MOFs were characterized using a SEM (LEO FESEM 1530) and HRTEM (JEOL 2101F, JEOL Ltd.) with EDS line-scan and mapping analysis. To ascertain each bonding group and verify the oxidation states of the MOF materials, XPS was also carried out (K-Alpha XPS spectrometer, Thermo Scientific). N₂ adsorption/desorption isotherm with BET and Barrett-Joyner-Halenda (BJH) analysis were performed to clarify the specific surface area, porosity, and pore volume of the developed catalyst.

Electrochemical Characterization RDE Tests: A traditional half-cell system with three electrodes was utilized to explore the electrochemical activities of the MOF catalysts, where the three electrodes were a glassy carbon electrode (GCE), a saturated calomel electrode (SCE), and a platinum wire used as the working electrode, reference electrode, and counter electrode, respectively. The electrocatalytic activity toward the OER and HER was evaluated using catalyst-loaded NFEs or via the RDE technique using catalyst-coated GCEs. A CHI Electrochemical Station (Model 760D) was used for all electrochemical evaluations. The measurements were conducted from 0 to 0.85 V versus SCE at 1600 rpm of rotation speed for OER, and from -0.9 to -1.5 V versus SCE at 1600 rpm of rotation speed for HER, with a scan rate of 10 mV s⁻¹. Pure nitrogen gas was purged

for 30 min before OER and HER evaluations and all measurements were performed in a 0.1 M KOH solution. All measured potentials were adjusted to the RHE scale, according to the equation; $E_{\text{RHE}} = E_{\text{SCE}} + 0.241 + 0.059 \text{ pH}$. All measured polarization curves were iR-compensated (See details in the Supporting Information) prior to electrochemical testing, the GCE (diameter: 5 mm) was polished using alumina suspension (size: 0.05 μm) on a smooth polishing cloth to obtain a uniform and smooth GCE surface, then the polished GCE surface was ultrasonicated in Milli-Q water for a few seconds to remove any leftover alumina particles. The catalyst ink was prepared by combining 2 mg catalyst and 2 mg vulcan carbon (XC-72, VC) in 1.0 mL of pretreated Nafion solution (mixture of 10 mL IPA and 80 μL of 5 wt% Nafion, Ion Power), followed by ultrasonication for 60 min to obtain a homogeneous suspension. 20 μL of the as-prepared ink was dropped onto the GCE surface and dried in room temperature, achieving a loading of 0.2 mg cm^{-2} catalyst. Meanwhile, precious metal catalysts consisting of platinum on carbon (Pt/C, 28.8 wt% Pt) and iridium on carbon (Ir/C, 20 wt% Ir) were utilized as benchmark catalysts to compare the electrocatalytic performances and practical efficiency of the MOF catalysts.

Practical Nickel Foam Electrode Tests: The catalysts were also loaded onto NFEs and tested using the same three-electrode configuration described above, using the NFE as the working electrode. Prior to testing catalyst-loaded NFEs, a piece of nickel foam was cut into a 1 cm \times 2 cm size and washed in 2.0 M HCl via ultrasonication for 1 h to remove any oxidized nickel, followed by washing ultrasonically in acetone for 1 h to remove organic impurities on its surface. The catalyst ink was prepared by mixing 0.5 mg catalyst and 0.5 mg VC in a 1.0 mL pretreated Nafion solution (mixture of 10 mL isopropyl alcohol (IPA) and 80 μL of 5 wt% Nafion, Ion Power) followed by ultrasonication for 60 min to obtain a homogeneous ink mixture. Then, the mixture was drop-casted onto the dried NFE (active area: 1 cm^2) achieving the loading of 0.5 mg cm^{-2} catalyst. The cycling was typically conducted at 50 mV s^{-1} scan rate in N_2 -saturated electrolyte until the CV curve showed stable currents indicating a stable solid/liquid interface.

Electrochemical Stability Tests: CP evaluation was also carried out to verify practical stabilities of the MOF catalysts. First, catalyst-coated GCE was activated by cyclic voltammetry (≈ 40 cycles) in a nitrogen-saturated electrolyte. Then, CP testing was conducted at constant current densities, where 20 and -20 mA cm^{-2} were applied to achieve sufficient OER and HER potentials, respectively. In terms of measuring the electrochemical performances, OER and HER overpotentials of catalyst-coated GCEs were measured at 10 and -10 mA cm^{-2} , respectively, and OER and HER overpotentials of catalyst-loaded NFEs were measured at 30 and -30 mA cm^{-2} , respectively. For easier comparison of the OER and HER overpotentials, 1.23 V versus RHE (equilibrium potential for splitting water) and 0 V versus RHE were used as the standard potentials for OER and HER, respectively.

Supporting Information

Supporting Information is available from the Wiley Online Library or from the author.

Acknowledgements

W.A. and M.G.P. contributed equally to this work. The authors wish to acknowledge the support provided by the Natural Sciences and Engineering Research Council of Canada (NSERC) through grants to Waterloo Institute for Nanotechnology at the University of Waterloo. This research was also supported by the Soonchunhyang University Research Fund.

Conflict of Interest

The authors declare no conflict of interest.

Keywords

bifunctional electrocatalysts, hydrogen evolution reaction, metal-organic-framework, oxygen evolution reaction, water-splitting

Received: March 26, 2018

Revised: April 21, 2018

Published online: June 3, 2018

- [1] Y. Zheng, Y. Jiao, S. Qiao, A. Vasileff, *Angew. Chem., Int. Ed.* **2018**, 57, 2.
- [2] J. Liu, Y. Zheng, Y. Jiao, Z. Wang, Z. Lu, A. Vasileff, S. Z. Qiao, *Small* **2018**, 14, 1704073.
- [3] Y. Zheng, Y. Jiao, M. Jaroniec, S. Z. Qiao, *Angew. Chem., Int. Ed.* **2015**, 54, 52.
- [4] Y. P. Zhu, Y. Jing, A. Vasileff, T. Heine, S. Z. Qiao, *Adv. Energy Mater.* **2017**, 7, 1602928.
- [5] T. Zhang, M.-Y. Wu, D.-Y. Yan, J. Mao, H. Liu, W.-B. Hu, X.-W. Du, T. Ling, S. Z. Qiao, *Nano Energy* **2018**, 43, 103.
- [6] X. Jia, Y. Zhao, G. Chen, L. Shang, R. Shi, X. Kang, G. I. N. Waterhouse, L.-Z. Wu, C.-H. Tung, T. Zhang, *Adv. Energy Mater.* **2016**, 6, 1502585.
- [7] T. Y. Ma, J. L. Cao, M. Jaroniec, S. Z. Qiao, *Angew. Chem., Int. Ed.* **2016**, 55, 1138.
- [8] J. Zhang, L. Qu, G. Shi, J. Liu, J. Chen, L. Dai, *Angew. Chem., Int. Ed.* **2016**, 55, 2230.
- [9] B. Y. Xia, Y. Yan, N. Li, H. B. Wu, X. W. Lou, X. Wang, *Nat. Energy* **2016**, 1, 15006.
- [10] Z. Li, M. Shao, L. Zhou, R. Zhang, C. Zhang, M. Wei, D. G. Evans, X. Duan, *Adv. Mater.* **2016**, 28, 2337.
- [11] A. Mahmood, W. Guo, H. Tabassum, R. Zou, *Adv. Energy Mater.* **2016**, 6, 1600423.
- [12] L. Han, X. Y. Yu, X. W. Lou, *Adv. Mater.* **2016**, 28, 4601.
- [13] S. You, X. Gong, W. Wang, D. Qi, X. Wang, X. Chen, N. Ren, *Adv. Energy Mater.* **2016**, 6, 1501497.
- [14] X. F. Lu, P. Q. Liao, J. W. Wang, J. X. Wu, X. W. Chen, C. T. He, J. P. Zhang, G. R. Li, X. M. Chen, *J. Am. Chem. Soc.* **2016**, 138, 8336.
- [15] K. Jayaramulu, J. Masa, O. Tomanec, D. Peeters, V. Ranc, A. Schneemann, R. Zboril, W. Schuhmann, R. A. Fischer, *Adv. Funct. Mater.* **2017**, 27, 1700451.
- [16] T. Y. Ma, S. Dai, M. Jaroniec, S. Z. Qiao, *J. Am. Chem. Soc.* **2014**, 136, 13925.
- [17] J. Nai, B. Y. Guan, L. Yu, X. W. D. Lou, *Sci. Adv.* **2017**, 3, e1700732.
- [18] J. Wang, F. Xu, H. Jin, Y. Chen, Y. Wang, *Adv. Mater.* **2017**, 29, 1605838.
- [19] J. Masa, P. Weide, D. Peeters, I. Sinev, W. Xia, Z. Sun, C. Somsen, M. Muhler, W. Schuhmann, *Adv. Energy Mater.* **2016**, 6, 1502313.
- [20] J. Ren, M. Antonietti, T.-P. Feller, *Adv. Energy Mater.* **2015**, 5, 1401660.
- [21] M. G. Park, D. U. Lee, M. H. Seo, Z. P. Cano, Z. Chen, *Small* **2016**, 12, 2707.
- [22] D. U. Lee, M. G. Park, H. W. Park, M. H. Seo, X. Wang, Z. Chen, *ChemSusChem* **2015**, 8, 3129.
- [23] D. U. Lee, M. G. Park, Z. P. Cano, W. Ahn, Z. Chen, *ChemSusChem* **2018**, 11, 406.
- [24] X. Cui, S. Yang, X. Yan, J. Leng, S. Shuang, P. M. Ajayan, Z. Zhang, *Adv. Funct. Mater.* **2016**, 26, 5708.
- [25] Y. Hou, Z. Wen, S. Cui, S. Ci, S. Mao, J. Chen, *Adv. Funct. Mater.* **2015**, 25, 872.
- [26] J. Fu, Z. P. Cano, M. G. Park, A. Yu, M. Fowler, Z. Chen, *Adv. Mater.* **2017**, 29, 1604685.
- [27] J. Fu, F. M. Hassan, C. Zhong, J. Lu, H. Liu, A. Yu, Z. Chen, *Adv. Mater.* **2017**, 29, 1702526.

- [28] Y. Jiang, Y.-P. Deng, J. Fu, D. U. Lee, R. Liang, Z. P. Cano, Y. Liu, Z. Bai, S. Hwang, L. Yang, D. Su, W. Chu, Z. Chen, *Adv. Energy Mater.* **2018**, 1702900.
- [29] W. Liu, J. Zhang, Z. Bai, G. Jiang, M. Li, K. Feng, L. Yang, Y. Ding, T. Yu, Z. Chen, A. Yu, *Adv. Funct. Mater.* **2018**, *28*, 1706675.
- [30] S. Gadipelli, T. Zhao, S. A. Shevlin, Z. Guo, *Energy Environ. Sci.* **2016**, *9*, 1661.
- [31] X.-Y. Yu, Y. Feng, B. Guan, X. W. Lou, U. Paik, *Energy Environ. Sci.* **2016**, *9*, 1246.
- [32] X. Y. Yu, L. Yu, H. B. Wu, X. W. Lou, *Angew. Chem., Int. Ed.* **2015**, *54*, 5331.
- [33] O. N. Risset, E. S. Knowles, S. Ma, M. W. Meisel, D. R. Talham, *Chem. Mater.* **2012**, *25*, 42.
- [34] C. L. Carvalho, A. T. Silva, L. J. Macedo, R. A. Luz, J. M. Moita Neto, U. P. Rodrigues Filho, W. Cantanhede, *Int. J. Mol. Sci.* **2015**, *16*, 14594.
- [35] Y. Liao, K. Pan, Q. Pan, G. Wang, W. Zhou, H. Fu, *Nanoscale* **2015**, *7*, 1623.
- [36] F. Calle-Vallejo, N. G. Inoglu, H.-Y. Su, J. I. Martínez, I. C. Man, M. T. M. Koper, J. R. Kitchin, J. Rossmeisl, *Chem. Sci.* **2013**, *4*, 1245.
- [37] J. Suntivich, K. J. May, H. A. Gasteiger, J. B. Goodenough, Y. Shao-Horn, *Science* **2011**, *334*, 1383.
- [38] F. Calle-Vallejo, O. A. Díaz-Morales, M. J. Kolb, M. T. M. Koper, *ACS Catal.* **2015**, *5*, 869.
- [39] M. H. Seo, H. W. Park, D. U. Lee, M. G. Park, Z. Chen, *ACS Catal.* **2015**, *5*, 4337.
- [40] J. K. Easton, J. - *Water Pollut. Control Fed.* **1967**, *39*, 1621.
- [41] M. Kuang, Q. Wang, P. Han, G. Zheng, *Adv. Energy Mater.* **2017**, *7*, 1700193.
- [42] D. Y. Chung, S. W. Jun, G. Yoon, H. Kim, J. M. Yoo, K. S. Lee, T. Kim, H. Shin, A. K. Sinha, S. G. Kwon, K. Kang, T. Hyeon, Y. E. Sung, *J. Am. Chem. Soc.* **2017**, *139*, 6669.
- [43] Y. Zheng, Y. Jiao, L. H. Li, T. Xing, Y. Chen, M. Jaroniec, S. Z. Qiao, *ACS Nano* **2014**, *8*, 5290.
- [44] Y. Yang, Z. Lun, G. Xia, F. Zheng, M. He, Q. Chen, *Energy Environ. Sci.* **2015**, *8*, 3563.
- [45] J. Deng, P. Ren, D. Deng, X. Bao, *Angew. Chem., Int. Ed.* **2015**, *54*, 2100.
- [46] Y. Liu, H. Yu, X. Quan, S. Chen, H. Zhao, Y. Zhang, *Sci. Rep.* **2014**, *4*, 6843.
- [47] M. Ye, M. Wang, D. Zheng, N. Zhang, C. Lin, Z. Lin, *Nanoscale* **2014**, *6*, 3576.
- [48] H. W. Park, D. U. Lee, M. G. Park, R. Ahmed, M. H. Seo, L. F. Nazar, Z. Chen, *ChemSusChem* **2015**, *8*, 1058.
- [49] X. Xu, H. Liang, F. Ming, Z. Qi, Y. Xie, Z. Wang, *ACS Catal.* **2017**, *7*, 6394.
- [50] D. Friebe, M. W. Louie, M. Bajdich, K. E. Sanwald, Y. Cai, A. M. Wise, M. J. Cheng, D. Sokaras, T. C. Weng, R. Alonso-Mori, R. C. Davis, J. R. Bargar, J. K. Nørskov, A. Nilsson, A. T. Bell, *J. Am. Chem. Soc.* **2015**, *137*, 1305.